Photothermal liquid release from arrayed Au nanorod/hydrogel composites for chemical stimulation

Sang-Woo Seo, Youngsik Song, and Hojjat Rostami Azmand

Department of Electrical Engineering, The City College of New York, 160 Convent Avenue, New York, NY 10031, USA

Email: swseo@ccny.cuny.edu

Abstract

Controlled photothermal actuation of liquid release is presented using periodically arrayed hydrogel columns in a macroporous silicon membrane. Thermo-responsive hydrogel is mixed with Au nanorods, and surface plasmon-induced local heating by near-infrared (NIR) light is utilized as an actuation method. We adopted theoretical modeling, which treats the hydrogel as a poro-viscoelastic medium to understand the mechanical and liquid transport properties of the hydrogel. To demonstrate the feasibility of the liquid release control using NIR light, we first characterized the temperature response of Au nanorod embedded hydrogel in the silicon membrane using its optical transmission to confirm the successful device fabrication. Next, the liquid release characteristics from the structure were studied using fluorescent imaging of fluorescein dye solution while pulsed NIR light was illuminated on the structure. We successfully demonstrate that the liquid release can be controlled using remote NIR illumination from the presented structure. Considering the periodically arrayed configuration with high spatial resolution, this will have a potential prospect for optically-addressable chemical release systems, which benefit retina prosthesis interfaces.

Keywords: p-NiPAAm hydrogel, chemical stimulation, photothermal, macroporous silicon, Au nanorods.

1. Introduction

Neural prosthetic devices have been employed to support disabled people to control their damaged body functions and improve their quality of life. For example, success has been realized in the development of cochlear prostheses [1], which bypass damaged hair cells by using direct electrical stimulation of the auditory nerve, and deep brain electrical stimulation [2], which has been beneficial to patients in decreasing the tremors associated with neurodegenerative disorders. Many of the current neural prostheses are based on electrical stimulation using microelectrodes. This method is based on applying electrical currents to excitable cells to restore sensory functions. However, to restore vision loss, the prosthetic retina based on electrical stimulations requires a unique level of sophistication to achieve the high spatial resolution of cellular stimulation for functional improvement in vision [3]. The main challenge comes from the complex sensory elements in the vision system compared to other body sensory systems. For example, the healthy eye has millions of photoreceptors and neuron cells to receive incoming light images and produce signals that create meaningful visual perception.

It is well known that complex information transfer in neural cells is primary through biochemical reactions. Localized chemical stimulation has been proposed to mimic the synaptic action of natural neural information processes and migrate the limitations of electrical stimulations [4-6]. For example, a micromachined silicon substrate with a circular aperture of 5 to 10 μm was used for chemical stimulation [7]. A microfluidic reservoir in the silicon under the aperture is connected to an external syringe pump using tubes to control neurotransmitter ejection through the aperture. Individually addressable 2 x 2 microtube arrays were presented to deliver controlled patterned neurotransmitters [8]. Nano/micropipettes constructed in a microscope configuration were utilized to modulate neuronal activities using controlled chemical release with the precise position [6, 9]. Biomimetic stimulations of the retina with neurotransmitters are also demonstrated. A chemical synapse chip with eight microfluidic ports was proposed to deliver spatially patterned neurotransmitter ejection [10].

While the feasibility and potential advantages of using chemical stimulations have been demonstrated, there are still engineering challenges that need to be developed for the successful transition of this approach with high spatial and temporal stimulation. These include providing a large number of stimulation sites for high-resolution stimulations and developing an independent actuation mechanism to control precise chemical release from different stimulation sites without complex physical interconnections.

We present photothermal actuation of Au nanorod embedded poly N-isopropyl acrylamide (p-NIPAAm) hydrogel columns in a macroporous silicon membrane by near-infrared (NIR) light to overcome those challenges in this paper. P-NIPAAm based hydrogel exhibits reversible phase transition at its lower critical solution temperature (LCST), and the LCST is readily controlled by copolymerizing with different monomers [11]. During the phase transition, p-NIPAAm hydrogel shows a reversible transition in optical, physical, and chemical properties, which creates great interest in biomedical applications such as actuators [12], drug delivery [13], and tissue engineering [14]. By incorporating Au nanorods as dopants during the hydrogel synthesis, plasmon-assisted heating can be utilized to remote control the reversible hydrogel properties [15]. Furthermore, the micron-scale hydrogel columns formed within pores allow fast, reversible photothermal actuation. Individual pores are physically separated and configured as vertically aligned microfluidic channels containing light-actuated hydrogels. This proposed structure provides new perspectives of high-density fluidic channels, which are significantly different from the conventional chemical stimulation approaches. We show that liquid release from the arrayed hydrogel columns can be rapidly controlled by light. Our approach can be implemented into remote drug release systems that can benefit applications in the area of chemical stimulations of neuronal networks requiring high spatiotemporal resolution of drug release.

2. Design and operation

P-NIPAAm hydrogel forms three-dimensional polymer networks with reversible hydrophilicity and hydrophobicity at its LCST. When the hydrogel is heated above its LCST, it shrinks and releases liquid contents. Fig. 1 shows an example of the temperature response of a bulk p-NIPAAm hydrogel used in our device structure. Bulk p-NIPAAm hydrogel was first saturated with water and placed on a temperature-controlled heating block. A thin glass slide was placed on the top of the hydrogel to visualize liquid oozing behavior from the hydrogel, and the resulting water trace was monitored by a digital camera. Its LCST was measured at around 30^{o}C. When the hydrogel is below LCST, there was no noticeable change in the liquid oozing behavior from the hydrogel. As the temperature reaches its LCST, the transparent hydrogel starts to expel its water content and turns opaque. Utilizing this unique temperature response, we demonstrate photothermal actuation of controlled liquid release in Au nanorod mixed p-NIPAAm hydrogels, which are spatially confined within an array of pores in a micrometer scale.

Fig. 2(a) shows a schematic structure of a porous membrane device. For this demonstration, we utilized a macroporous porous silicon structure. Two-dimensional pores are arrayed. The pitch period is 12 μm. The membrane thickness is about 400 μm. Pore diameters are measured to 11 μm on the front side and 9 μm on the back side, as shown in Fig. 2(b). Au nanorod mixed p-NIPAAm hydrogel was filled within the pore array, forming a hydrogel column array. Au nanorods act as photothermal transducers, which convert near-infrared optical energy into thermal energy. Based on the unique temperature characteristics, p-NIPAAm hydrogel goes through phase-transition at its LCST. At the temperature above the LCST, hydrogel volume shrinks, and liquid inside the hydrogel is released. We show that arrayed hydrogel columns can be rapidly controlled by light in this paper. This will benefit designing novel light-directed chemical stimulation systems. To understand the physical operation of the membrane device, we performed a theoretical study based on a poro-viscoelastic model, in which the mechanics of hydrogel is coupled with the liquid transport and poro-viscoelastic behavior within the hydrogel polymer networks.

Fig. 2(c) shows the schematic of a single pore column that is used for our theoretical study. Following the modeling approach by Caccavo et al. [16], mass and linear momentum balance equations are incorporated into constitutive equations, including elastic properties of the hydrogel. Hydrogel volumetric change is related to a constraint of liquid concentration to the hydrogel deformation. Liquid and hydrogel polymer are treated as incompressible, while hydrogel volume can be varied due to its liquid content.

The modeling has been implemented into COMSOL Multiphysics through a mathematical interface using weak forms. 2D-axisymmetric geometry was used to represent hydrogel column filled within a pore. The initial hydrogel diameter and length filled within a pore are 10 μm and 400 μm, respectively. Material parameters summarized in Table 1 are used for the simulation [17].

As boundary conditions, Γ_1 represents a 2D-axisymmetric boundary with no flux of water. Γ_2 represents the bottom side of the pore with a fixed boundary. This assumes that light-induced hydrogel volume change is small on the bottom of the pore. Γ_3 and Γ_4 represent the boundaries of the top and side of the pore, where hydrogel can move freely within the pore boundary and contacts external water.

Free swelling of hydrogel was first calculated by immersing the simulation domain in water to find equilibrium water content percentage. Water mass fraction within the hydrogel was varied until the swelling volume change of hydrogel was negligible. In our experiment, the membrane device was stored in water before starting our experiment. Therefore, the hydrogel within the device was fully saturated and balanced with water content without further deformation. Based on the material parameters summarized in Table 1, the water mass fraction in equilibrium was calculated as 0.97. We used this value as an initial condition and performed the liquid release behavior of the hydrogel confined within the pore. Fig. 3 shows a calculated liquid release when the top portion of the hydrogel is shrunk with different depths as a function of time. When NIR light is illuminated to the top of the pore, temperature increase through Au-nanorod assisted photothermal effect will be first initiated from the top portion of the hydrogel. This will cause a decrease in the hydrogel volume from the top portion. On the contrary, when the NIR light is turned off, the temperature is decreased, and the hydrogel volume will be restored. It is expected that the shrink depth will be related to NIR light intensity and duration. To mimic this behavior, a simple model of hydrogel volume change is applied on the top portion of the hydrogel with different depths as a function of time for a boundary condition. The depth transition follows two rectangular pulses with 3 seconds of duration, 1 second of transition, and 5 seconds of separation. Fig. 3 shows a calculated liquid release from the hydrogel for the liquid diffusivity (Diff) of 1 x

10^{-7} m^2/sec. As expected, more liquid is ejected from the hydrogel when it shrinks more. Fig. 4 shows a calculated liquid release from the hydrogel with various liquid diffusivities at 7 µm of the shrinking depth. The results show that diffusivity of the liquid affects the release behavior significantly and creates some accumulated delay on the response if the release actuation is applied too soon before the hydrogel reaches its equilibrium condition. The cross-linking density during hydrogel synthesis can be a parameter to adjust the diffusivities of water and small solutes [18]. Fig. 5 shows liquid concentration plots within the hydrogel for different diffusivities. Fig. 5(a) shows an initial liquid concentration before the hydrogel shrinks. Fig. 5(b-d) show comparative liquid concentration distributions when hydrogel shrinks and reaches 7 µm depth at t = 5 sec. It shows that the liquid with faster diffusivity can be quickly redistributed and allow more liquid to be released, while the liquid with slow diffusivity still has non-uniform distribution within the hydrogel. This will contribute to the different release characteristics, as shown in Fig. 4.

3. Materials and fabrications

Chloroauric Acid ($HAuCl_4$), Hexadecyltrimethylammonium Bromide (CTAB), Sodium Borohydride ($NaBH_4$), Dimethyl Sulfoxide (DMSO), and 2-Hydroxy-2-methylpropiophenone (Darocur 1173) were purchased from Sigma Aldrich, USA. Fluorescein dye, Silver Nitrate ($AgNO_3$), and N-isopropyl acrylamide (NIPAAm) were purchased from TGI America, USA. N,N'-Methylene-bis-acrylamide (MBAAm), Ascorbic Acid ($C_6H_8O_6$), and Polyvinylpyrrolidone (PVP) were purchased from VWR, USA. Deionized (DI) water (Reagent Grade. ~ 18MΩ/cm, Electron Microscopy Sciences, Inc., USA) was used for all solution preparation.

3.1 Synthesis of gold nanorods

Gold (Au) nanorods were synthesized by the seed meditated method as described [15]. Briefly, Au seed solution was prepared by diluting 0.25 mL 10 mM $HAuCl_4$ in 9.75 mL 0.1 M CTAB, and followed by injection of ice-cold 600 μL 10 mM $NaBH_4$ to the mixture of $HAuCl_4$ and CTAB at the stirring speed of 1000 rpm. The Au seed solution was aged for 2 hours without stirring at 25 ºC. Next, Au nanorods were synthesized by adding 85 μL 10 mM $AgNO_3$ in 9.5 mL 0.1M CTAB solution, followed by the addition of 500 μL 10 mM $HAuCl_4$ and 55 μL 0.1M ascorbic acid. Finally, freshly prepared 12 μL Au seed solution was injected and left for 2 hours at 27 ºC. A pellet of Au nanorods was obtained from Au nanorods suspension by centrifugation at 10000 rpm for 30 minutes. The transmission characteristics of Au nanorods were measured without further process after synthesis. Figure 6 shows transmission spectra of as-synthesized Au nanorods suspension for 10mm path length. The measured optical absorption at 815nm, where we performed our photothermal experiments, is around 1.76 cm^{-1} for as-synthesized concentration. It is expected that as-synthesized suspension has about 1 mg of Au nanorods in 10ml suspension, assuming 100% yield [19]. There are two distinct peaks in the absorbance spectra. The peak near 507 nm is due to transverse resonance mode, and the peak in NIR wavelength at 815nm is longitudinal resonance mode.

3.2 UV curable Au nanorod/p-NIPAAm hydrogel composite

As-synthesized Au nanorods are terminated with positively charged CTAB, which often tend to aggregate and result in non-uniform dispersion in the p-NIPAAm hydrogel solution. In order to obtain uniformly dispersed Au nanorods in UV curable p-NIPAAm solution, Au nanorods were functionalized with PVP surfactant as follows. First, Au nanorod precipitate obtained from 20mL of as-synthesized Au nanorod suspension was re-suspended in 2 wt. % PVP solution for 24 hours to convert to PVP functionalized Au nanorods. Again, PVP functionalized Au nanorods as a pellet were collected by centrifugation at 10000 rpm for 30 minutes. The pellet of PVP functionalized Au nanorods was re-suspended in the mixture of 0.2 g of NIPAAm monomer, 0.01g of MBAAm crosslinker, and 20 µL Darocur 1173 UV initiator in 1mL DMSO solution. The concentration of Au nanorods for 1mL DMSO solution is 20 times higher than as-synthesized suspension, which expects to increase the absorption at a similar rate. The resulting hydrogel solution was stable for several weeks without visible Au nanorod aggregations.

To study the photothermal response of Au nanorod mixed p-NIPAAm hydrogels, a bulk p-NIPAAm hydrogel shown in Fig. 7(a) was prepared. The prepared Au nanorod mixed hydrogel solution was poured in a Teflon mold and cured by 345nm UV light for around 2 min. Finally, the cured hydrogel was soaked in DI water to replace DMSO with water for 24 hours. The fabricated bulk p-NIPAAm hydrogel shows uniform dispersion of Au nanorods without aggregation. To quantify the temperature change as a function of NIR illumination at 815nm, NIR light beam is collimated and illuminated on the fabricated bulk hydrogel. The beam diameter was measured at around 5.3 mm. Fig. 7(b) shows an example of the measured temperature profile by the FLIR i7 compact infrared (IR) thermal imaging camera (FLIR system, USA). Fig. 7(c) shows temperature change as a function of NIR illumination time and optical power on bulk Au nanorod/p-NIPAAm hydrogel. The temperature at the illumination spot increased gradually with illumination time and saturated at a certain maximum temperature for a given optical power. As expected, higher optical power produces higher temperature change.

3.3 Porous silicon membrane embedded with Au nanorod/p-NIPAAm hydrogel composite

Periodically arranged, macroporous silicon substrates were purchased from Smart Membranes, Germany. The pore diameter, depth, and pitch distance are 5 µm, 470 µm, and 12 µm, respectively. The size of the sample was 8mm x 8mm. The back side of silicon was lapped by two-step lapping process. First lapping process with 6 µm alumina slurry to open pores on the back side, and second lapping process with 0.25 µm alumina slurry to smoothen the surface. The pores of the membrane sample were enlarged by repeating thermal-oxidation and buffered oxide etching processes, resulting in smoother pore structures. The resulting silicon membrane has slightly different sizes of pores on the front and back sides shown in Fig. 2(b). The membrane thickness was measured at around 400 µm.

Before filling with Au nanorods incorporated p-NIPAAm hydrogel solution in pores, the silicon membrane was cleaned with Piranha solution, a 3:1 mixture of concentrated sulfuric acid (H_2SO_4) with hydrogen peroxide (H_2O_2) for 10 minutes, and rinsed with DI water.

Followed by the degassing-assisted pore filling approach [20], we filled the prepared hydrogel solution into the macroporous membrane. A polydimethylsiloxane (PDMS) block with a 5 mm deep, 9 mm x 9 mm square chamber was prepared for this process. Dow Corning Sylgard 182 elastomer and curing agent were mixed with a weight ratio of 10:1 and degassed for 30 min to remove air bubbles. Next, the mixture was poured on a Teflon replica mold to make the PDMS block with a square chamber. To have a flat surface on the square chamber, a square silicon piece was mounted using Apiezon wax on the top of the Teflon square pillar, where the chamber is created. Once the PDMS was fully cured at 80 ^{o}C for 3 hours, the PDMS block was released.

To embed Au nanorod mixed hydrogel within a porous membrane sample, the prepared silicon membrane was placed on the square chamber of the PDMS block and degassed for 30 minutes in a vacuum. Then, the prepared Au nanorod/hydrogel solution filled the porous membrane sample in the PDMS chamber and was cured using 345nm UV light for 5 minutes. After the hydrogel mixture was polymerized, the membrane device was carefully taken out from the PDMS mold, and the hydrogel outside of the membrane was removed by a razor blade. Finally, the membrane device was soaked in DI water for at least 24 hours before the following actuation experiments.

4. Result and discussion

To demonstrate the liquid release by photothermal actuation of Au nanorod/hydrogel composite columns in the macroporous silicon membrane by NIR light, a custom microscope setup as shown in Fig. 8(a) was constructed. The setup accommodates fluorescent imaging of the emission spectra of fluorescein using ultraviolet (UV) light at 475nm as excitation light and pulsed NIR light illumination at 815nm on the top of a sample with two sets of appropriate dichroic filters. The resulting images were captured from a digital microscope camera. In addition, the setup has a white light illumination under the stage to characterize optical transmission through the membrane device. The membrane device was mounted in a temperature-controlled heating block, as shown in Fig 8(a). To visualize the liquid actuation from the device, 0.2% fluorescein solution was prepared in water and loaded on the bottom of the device as a reservoir. Mineral oil was placed on the top of the sample to prevent liquid evaporation during the experiment. Finally, a glass cover slide was placed on the top of the block. Fig. 8(b) shows an image of the microscope setup with the heating block and a membrane sample held by a tweezer in a sub-picture. Fig. 8(c) shows a fluorescent image from the top of a membrane sample during the experiment. Bright fluorescent signals were clearly observed through arrayed pores. Utilizing an oil-water interface, we were able to minimize diffusion of fluorescein to adjacent pores of the membrane device and monitor stable fluorescent imaging through arrayed pores when there were no external perturbations.

First, light transmission through the fabricated membrane device was measured. Since the optical opaqueness of the hydrogel is correlated with its volumetric change [21], this indirect optical measurement result confirms that the hydrogel is successfully embedded within the porous structure and will experiences phase transition at its LCST. For this measurement, white broadband light was illuminated from the bottom of the membrane device, and its optical transmission through pores was recorded by the camera as a function of the temperature in the heating block. Fig. 9 shows the measured optical transmission as a function of temperature cycles in the heating block (Supplementary material, Video 1 for image stacks when temperature increases). It is clearly observed that the hydrogel phase transition occurs at around 30 ^{o}C. Similar to the temperature response of a bulk p-NIPAAm hydrogel below LCST, the hydrogel was relatively transparent and allowed light transmission through the membrane. As the temperature increased above the LCST, hydrogel turned opaque, and light transmission was blocked. No physical damage to the embedded hydrogels was observed even after the repeated temperature cycling measurements. Considering that the pore diameter and length are around 5 µm and 400 µm, the embedded hydrogel is stably retained within the pores without falling off from the membrane structure.

To demonstrate optically induced liquid actuation, pulsed NIR light at 815 nm with a peak power of 100mW was applied on the top of the membrane device. It is expected that pulsed NIR light induces temperature increase inside hydrogel through plasmonic heating by Au nanorods. Considering the estimated light absorption coefficient of 35.2 cm^{-1} at 815nm for the Au nanorod/hydrogel composition used in the device, the photothermal volume actuation of the hydrogel will be effectively initiated from the top portion of the pore array. As expected from our simulation results, fluorescein solution from the hydrogel is released and accumulated on the top of the pore.

Fig. 10 shows the measured fluorescent signal intensity variation as a function of time. Repeatable actuation of p-NIPAAm hydrogel columns by the photothermal effect was observed. NIR light was modulated for this experiment with 7 seconds of on and 9 seconds of off cycles (Supplementary material, Video 2 during NIR laser on/off cycles). Average surface intensities were calculated from the measured fluorescent images. The insert images show the exemplary surface intensity profiles at NIR laser off and NIR laser on regions. We were able to observe the fluorescent signal modulation following the laser modulation rate. Since the hydrogel turns opaque when the temperature is above its LCST, the fluorescent signal from deep inside the pore will be weak, and the main contribution of the fluorescent signal increase is expected to be by the fluorescein solution released from the hydrogel. The fluorescent signal had a pattern of abrupt increase at the first 3 seconds and following slow saturation when NIR light turned on. When the NIR light turned off, the fluorescent signal decreased. When the next NIR light pulse actuations were applied, the overall signal characteristics were almost identical, but the pulse responses, including peak intensities, were gradually increased. Similar responses were predicted from our simulation result when the liquid release is limited by its large diffusion rate, as shown in Fig. 4. After the first pulse actuation, the released molecules are accumulated to affect the subsequent actuation response, which results in gradually increased peak intensities. The measured response trends agree with our simulation results.

Fig. 11 shows the measured fluorescent signals when the laser modulation parameters are varied. When the laser on-time was fixed at 2 seconds, we have observed that it took at least 5 seconds for the fluorescent response to reach its equilibrium condition, as shown in Fig. 11(a). Since the laser on-time was relatively short in this case, we did not see fluorescent signal saturation, and their response was abrupt. For a fixed off-time, as we increase the laser on-time, we expect that the hydrogel will shrink more and release more fluorescein. The measured fluorescent intensity shown in Fig. 11(b) was increased, and its saturation trend was observed for a longer laser on-time. When the laser on-time was linearly increased, the peak intensity change did not follow the linear increase. Following our simulation result shown in Fig. 3, if the shrink depth is linearly increased, the fluorescent signals resulting from release dye molecules expect to be linearly increased. This discrepancy requires further studies but might be due to non-linear photothermal volume changes. While the detailed optical to temperature modeling can be useful in future studies, the simple hydrogel volume-induced liquid release modeling can explain the current liquid release mechanism.

5. Conclusion

We have demonstrated the controlled liquid release utilizing photothermal actuation of Au nanorod embedded hydrogel confined in a macroporous silicon membrane. Temperature-sensitive p-NIPAAm hydrogel mixed with Au nanorods was embedded within microscale pores defined in a macroporous membrane, which represents three-dimensional microfluidic channels in a vertical direction. Plasmon-induced thermal heating of Au nanorods can be remotely controlled by NIR light and allows the actuation of p-NIPAAm hydrogel for the controlled liquid release from the pores. We have theoretically modeled the liquid release mechanism and experimentally demonstrated the feasibility of the liquid release through fluorescent dye imaging. Considering the arrayed fluidic ports formed by pores and the optical control approach, it has the potential to be implemented into novel drug release systems that require different release patterns of drugs with high spatial and temporal resolutions typically seen in many biological neural stimulation systems.

ACKNOWLEDGMENT

This work was supported by CUNY PSC-CUNY grant and National Science Foundation grant (NSF-1952469).

DATA AVAILABILITY

The data that support the findings of this study are available in the article or supplementary materials.

References

[1] B. S. Wilson and M. F. Dorman, "Cochlear implants: current designs and future possibilities," *J. Rehabil. Res. Dev.,* vol. 45, *(5),* pp. 695-730, 2008.

[2] A. M. Lozano, N. Lipsman, H. Bergman, P. Brown, S. Chabardes, J. W. Chang, K. Matthews, C. C. McIntyre, T. E. Schlaepfer and M. Schulder, "Deep brain stimulation: current challenges and future directions," *Nature Reviews Neurology,* vol. 15, *(3),* pp. 148-160, 2019.

[3] L. Yue, J. D. Weiland, B. Roska and M. S. Humayun, "Retinal stimulation strategies to restore vision: Fundamentals and systems," *Prog. Retin. Eye Res.,* vol. 53, pp. 21-47, 2016.

[4] P. G. Finlayson and R. Iezzi, "Glutamate stimulation of retinal ganglion cells in normal and s334ter-4 rat retinas: a candidate for a neurotransmitter-based retinal prosthesis," *Invest. Ophthalmol. Vis. Sci.,* vol. 51, *(7),* pp. 3619-3628, 2010.

[5] C. M. Rountree, A. Raghunathan, J. B. Troy and L. Saggere, "Prototype chemical synapse chip for spatially patterned neurotransmitter stimulation of the retina ex vivo," *Microsystems & Nanoengineering,* vol. 3, *(1),* pp. 1-12, 2017.

[6] W. Haq, J. Dietter, S. Bolz and E. Zrenner, "Feasibility study for a glutamate driven subretinal prosthesis: local subretinal application of glutamate on blind retina evoke network-mediated responses in different types of ganglion cells," *Journal of Neural Engineering,* vol. 15, *(4),* pp. 045004, 2018.

[7] M. C. Peterman, N. Z. Mehenti, K. V. Bilbao, C. J. Lee, T. Leng, J. Noolandi, S. F. Bent, M. S. Blumenkranz and H. A. Fishman, "The artificial synapse chip: a flexible retinal interface

based on directed retinal cell growth and neurotransmitter stimulation," *Artif. Organs,* vol. 27, *(11),* pp. 975-985, 2003.

[8] Y. Li, H. Tu, R. Iezzi, P. Finlayson and Y. Xu, "Development of individually-addressable parylene microtube arrays," *J Micromech Microengineering,* vol. 21, *(11),* pp. 115005, 2011.

[9] M. J. Aebersold, H. Dermutz, L. Demkó, J. F. S. Cogollo, S. Lin, C. Burchert, M. Schneider, D. Ling, C. Forró and H. Han, "Local Chemical Stimulation of Neurons with the Fluidic Force Microscope (FluidFM)," *ChemPhysChem,* vol. 19, *(10),* pp. 1234-1244, 2018.

[10] C. M. Rountree, J. B. Troy and L. Saggere, "Microfluidics-based subretinal chemical neuromodulation of photoreceptor degenerated retinas," *Invest. Ophthalmol. Vis. Sci.,* vol. 59, *(1),* pp. 418-430, 2018.

[11] S. J. Lue, C. Chen and C. Shih, "Tuning of lower critical solution temperature (LCST) of poly (N-isopropylacrylamide-co-acrylic acid) hydrogels," *Journal of Macromolecular Science, Part B,* vol. 50, *(3),* pp. 563-579, 2011.

[12] B. Salahuddin, H. Warren and G. M. Spinks, "Thermally actuated hydrogel bead based braided artificial muscle," *Smart Mater. Struct.,* vol. 29, *(5),* pp. 055042, 2020.

[13] Z. Li and J. Guan, "Thermosensitive hydrogels for drug delivery," *Expert Opinion on Drug Delivery,* vol. 8, *(8),* pp. 991-1007, 2011.

[14] P. J. Kondiah, Y. E. Choonara, P. P. Kondiah, T. Marimuthu, P. Kumar, L. C. Du Toit and V. Pillay, "A review of injectable polymeric hydrogel systems for application in bone tissue engineering," *Molecules,* vol. 21, *(11),* pp. 1580, 2016.

[15] Y. Song, H. R. Azmand and S. Seo, "Rapid photothermal actuation of light-addressable, arrayed hydrogel columns in a macroporous silicon membrane," *Sensors and Actuators A: Physical,* vol. 301, pp. 111729, 2020.

[16] D. Caccavo and G. Lamberti, "PoroViscoElastic model to describe hydrogels' behavior," *Materials Science and Engineering: C,* vol. 76, pp. 102-113, 2017.

[17] D. Caccavo, S. Cascone, G. Lamberti and A. A. Barba, "Modeling the drug release from hydrogel-based matrices," *Molecular Pharmaceutics,* vol. 12, *(2),* pp. 474-483, 2015.

[18] Y. Wu, S. Joseph and N. Aluru, "Effect of cross-linking on the diffusion of water, ions, and small molecules in hydrogels," *The Journal of Physical Chemistry B,* vol. 113, *(11),* pp. 3512-3520, 2009.

[19] N. D. Burrows, S. Harvey, F. A. Idesis and C. J. Murphy, "Understanding the seed-mediated growth of gold nanorods through a fractional factorial design of experiments," *Langmuir,* vol. 33, *(8),* pp. 1891-1907, 2017.

[20] S. Seo, A. N. Enemuo and H. R. Azmand, "Fast thermoresponsive optical membrane using hydrogels embedded in macroporous silicon," *IEEE Sensors Letters,* vol. 2, *(2),* pp. 1-4, 2018.

[21] C. Liu, J. Yu, G. Jiang, X. Liu, Z. Li, G. Gao and F. Liu, "Thermosensitive poly (N-isopropylacrylamide) hydrophobic associated hydrogels: optical, swelling/deswelling, and mechanical properties," *J. Mater. Sci.,* vol. 48, *(2),* pp. 774-784, 2013.

Figure Captions

Figure 1. Temperature characteristics of a bulk p-NIPAAm hydrogel.

Figure 2. (a) A schematic structure of a porous membrane device with Au nanorods/p-NIPAAm hydrogel composite. (b) Images of the front (left image) and back (right image) sides of the porous membrane used for the device. (c) A single pore column configuration used for our theoretical modeling.

Figure 3. Calculated liquid release characteristics when the top portion of the hydrogel column embedded in a pore is shrunk with different depths as a function of time.

Figure 4. Calculated liquid release characteristics when different diffusivities of the liquid are assumed for the same shrink depth as a function of time.

Figure 5. Liquid concentration (in mol/m^3) plots within the hydrogel for different diffusivities. (a) Initial concentration in equilibrium before hydrogel shrinks. (b) Diffusivity of 10^{-7} m^2/s. (c) Diffusivity of 10^{-9} m^2/s. (d) Diffusivity of 10^{-11} m^2/s when hydrogel shrinks.

Figure 6. Transmission spectra of as-synthesized Au nanorod suspension for 10 mm optical path length.

Figure 7. Photothermal response of a bulk p-NIPAAm hydrogel mixed with Au nanorods. (a) Image of a prepared bulk p-NIPAAm hydrogel mixed with Au nanorods. (b) Example image of temperature profile measurement using IR camera when NIR is illuminated on the hydrogel. (c) Measured temperature characteristics as a function of optical power and time.

Figure 8. (a) Schematic diagram of the custom-built measurement setup. (b) Image of the setup. (c) Example fluorescent image from the top of a membrane sample during the experiment.

Figure 9. Normalized optical transmission as a function of temperature cycles in the heating block. Insert images are shown at temperatures of 25 ºC and 41 ºC. (Supplementary material, Video 1 when temperature is increased).

Figure 10. Measured fluorescent signal intensity variation as a function of time when NIR light is illuminated on the device with 7 seconds of ON and 9 seconds of OFF cycles. Insert 2D surface images are shown at different time regions of NIR laser off and NIR laser on. (Supplementary material, Video 2 shows fluorescent imaging).

Figure 11. Measured fluorescent signal intensity variation when the laser modulation

parameters are varied. (a) laser on-time is 2 seconds with the variation of laser off-time. (b) laser off-time is 9 seconds with the variation of laser on-time.

Figure 1.

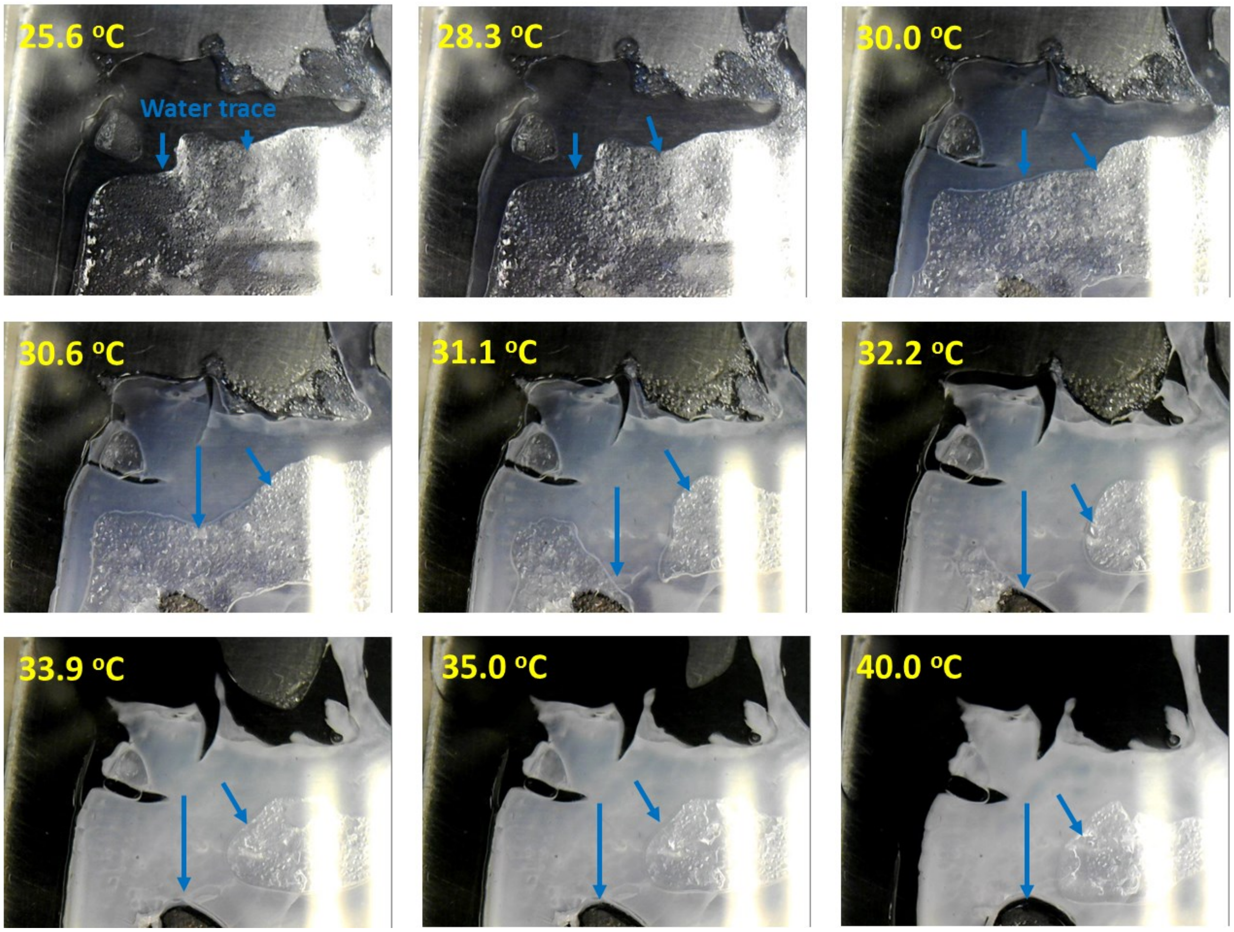

25.6 ^oC
Water trace
28.3 ^oC
30.0 ^oC
30.6 ^oC
31.1 ^oC
32.2 ^oC
33.9 ^oC
35.0 ^oC
40.0 ^oC

Figure 2.

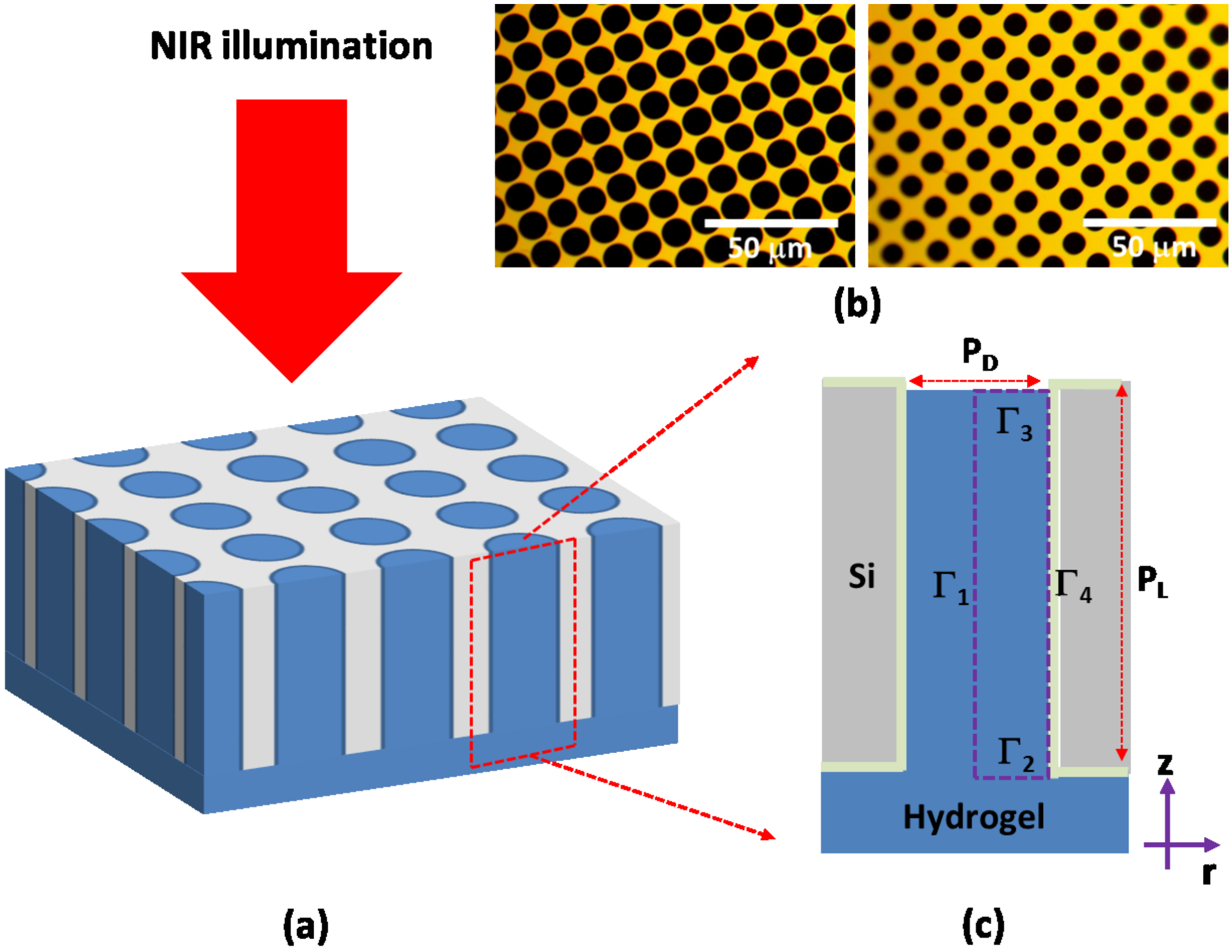
NIR illumination
50 μm
50 μm
(b)
P_D
Γ_3
Si
Γ_1
Γ_4
P_L
Γ_2
z
Hydrogel
r
(a)
(c)

Figure 3.

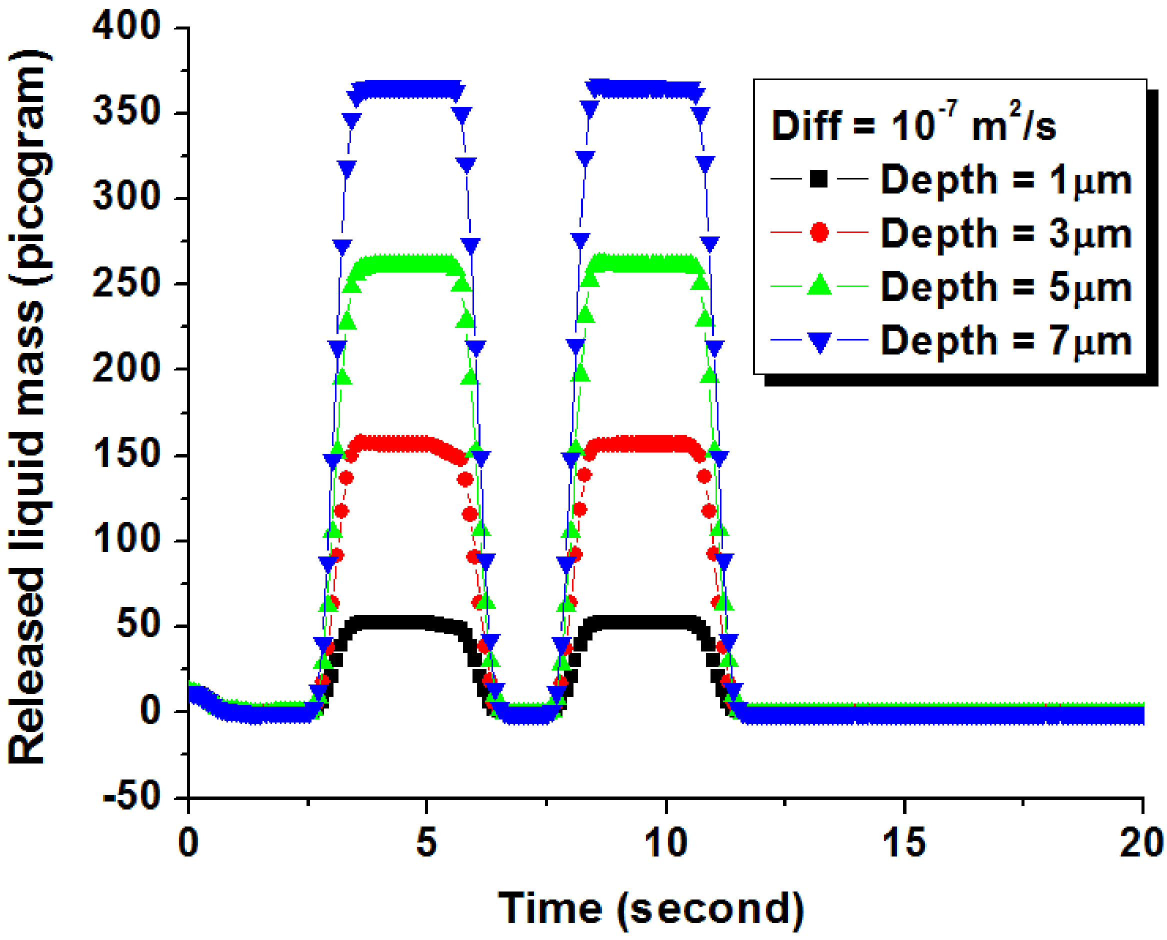

Released liquid mass (picogram)
400
350
300
250
200
150
100
50
0
-50
0
5
10
15
20
Time (second)
Diff = 10^{-7} m^2/s
Depth = 1μm
Depth = 3μm
Depth = 5μm
Depth = 7μm

Figure 4.

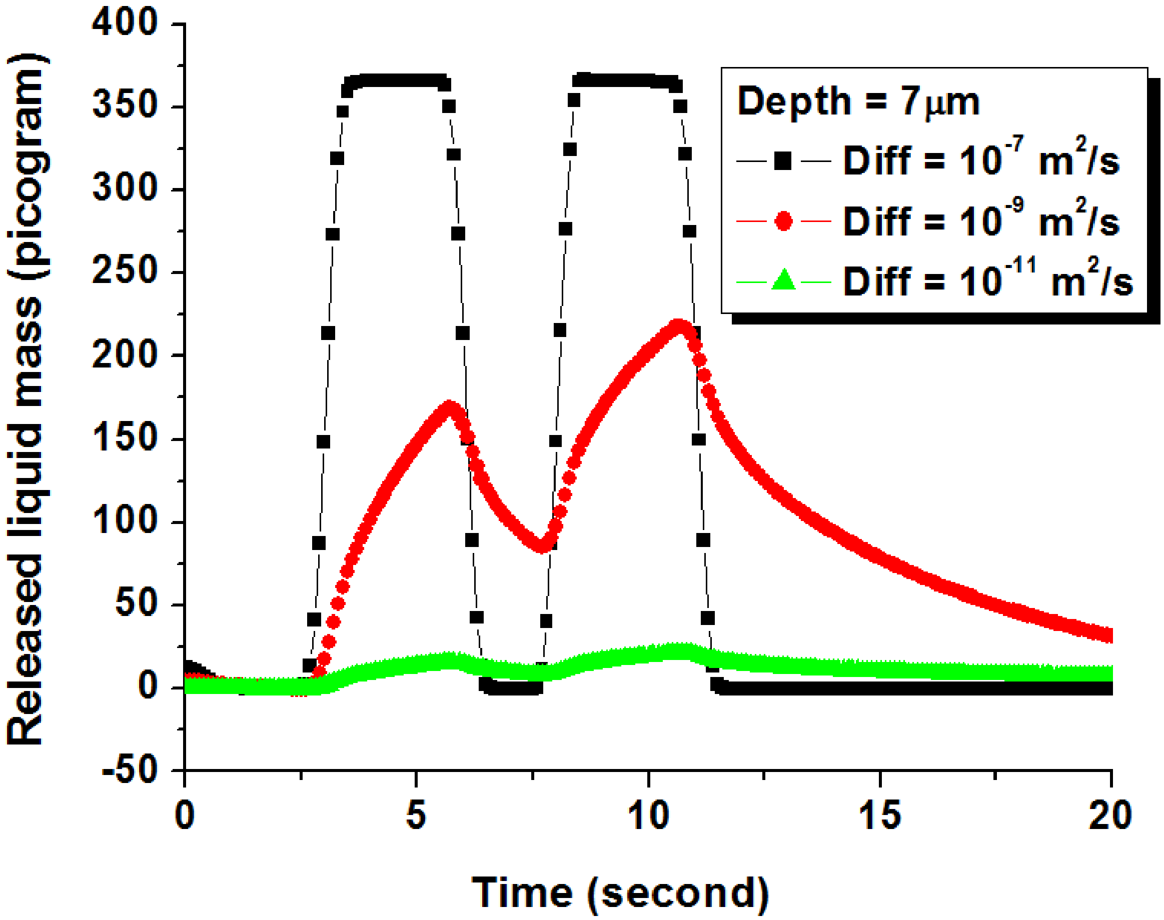

Released liquid mass (picogram)
400
350
300
250
200
150
100
50
0
-50
0
5
10
15
20
Time (second)
Depth = 7μm
Diff = 10^{-7} m^2/s
Diff = 10^{-9} m^2/s
Diff = 10^{-11} m^2/s

Figure 5.

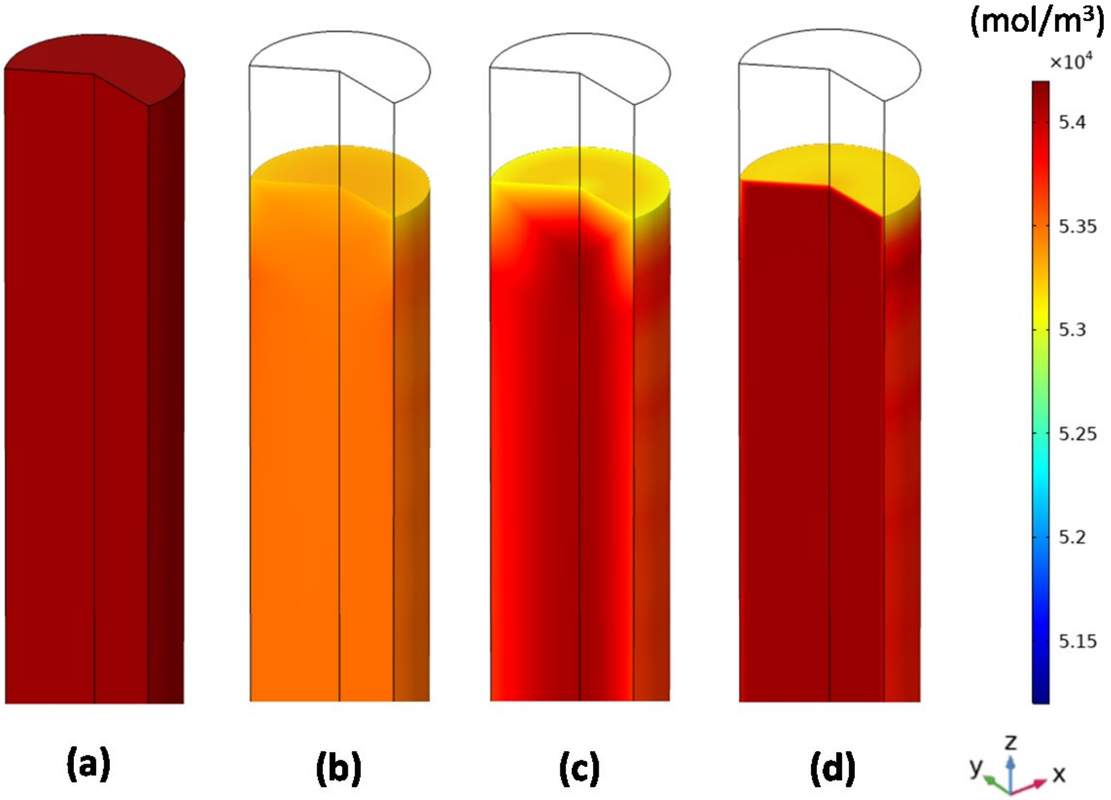

Figure 6.

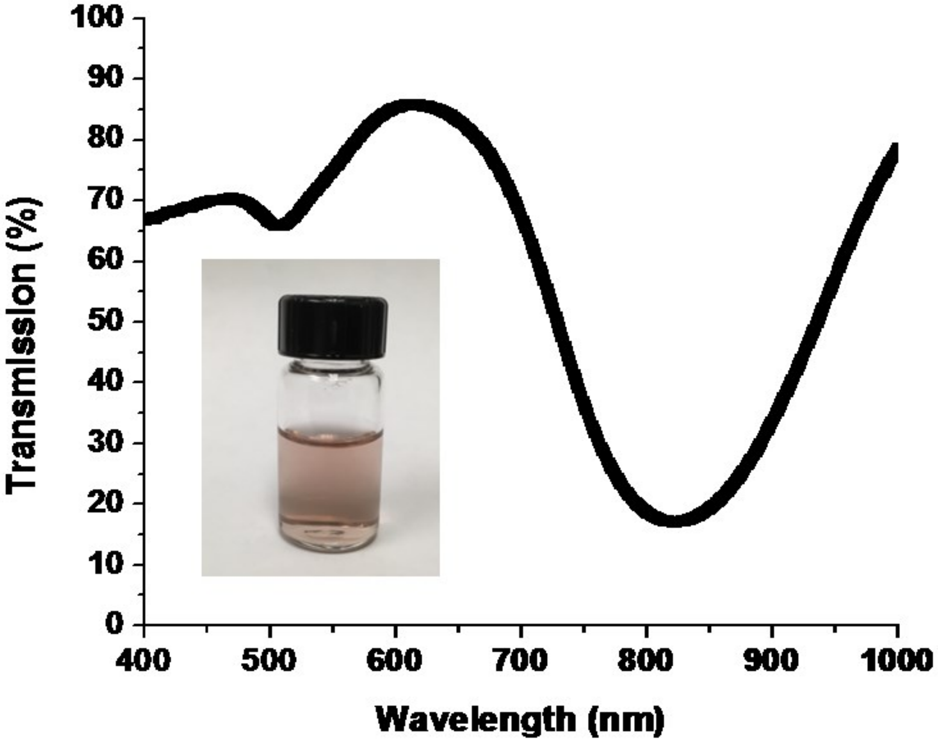

Transmission (%)
0
10
20
30
40
50
60
70
80
90
100
400
500
600
700
800
900
1000
Wavelength (nm)

Figure 7.

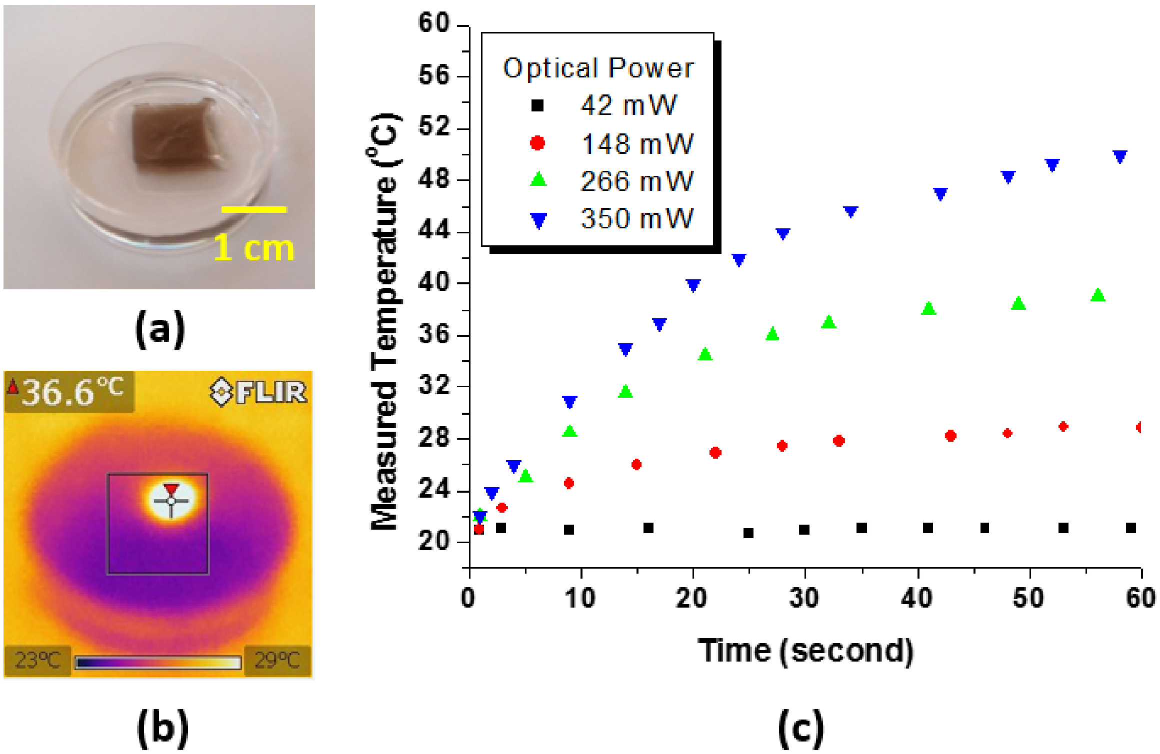
1 cm
(a)
36.6°C
FLIR
23°C
29°C
(b)
Optical Power
42 mW
148 mW
266 mW
350 mW
Measured Temperature (°C)
20
24
28
32
36
40
44
48
52
56
60
Time (second)
0
10
20
30
40
50
60
(c)

Figure 8.

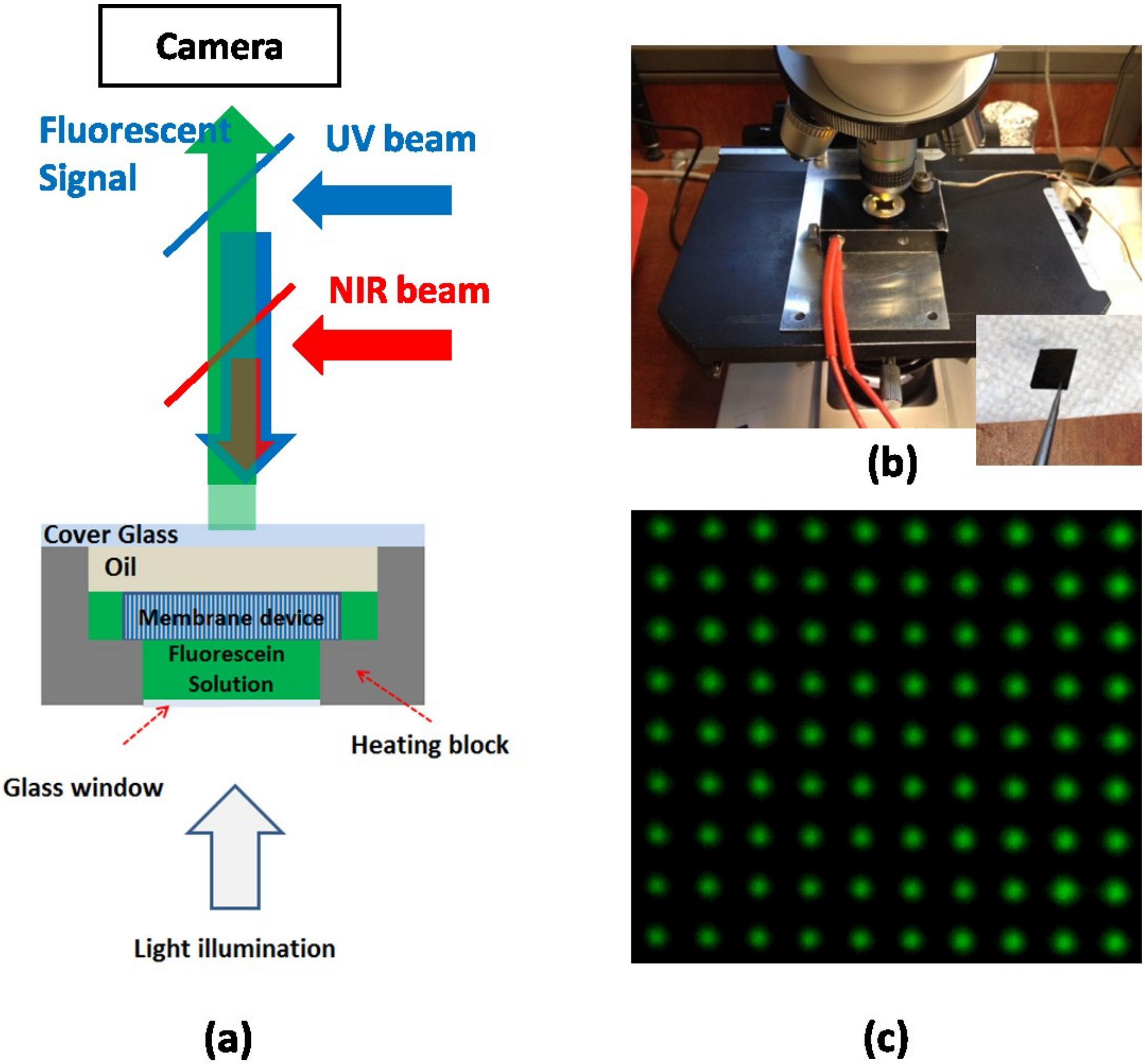
Camera
Fluorescent Signal
UV beam
NIR beam
Cover Glass
Oil
Membrane device
Fluorescein Solution
Glass window
Heating block
Light illumination
(b)
(a)
(c)

Figure 9.

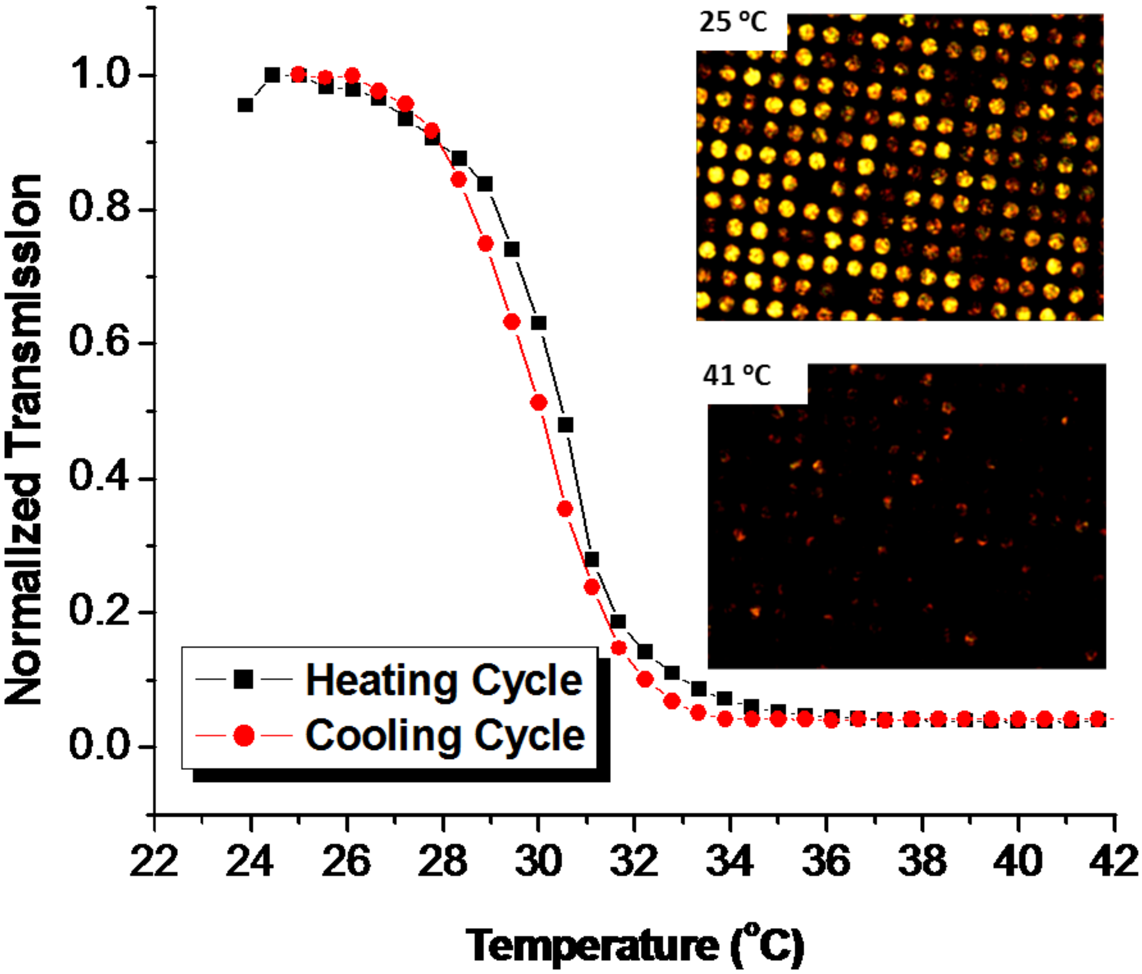

25 °C
41 °C
1.0
0.8
0.6
0.4
0.2
0.0
Normalized Transmission
Heating Cycle
Cooling Cycle
22
24
26
28
30
32
34
36
38
40
42
Temperature (°C)

Figure 10.

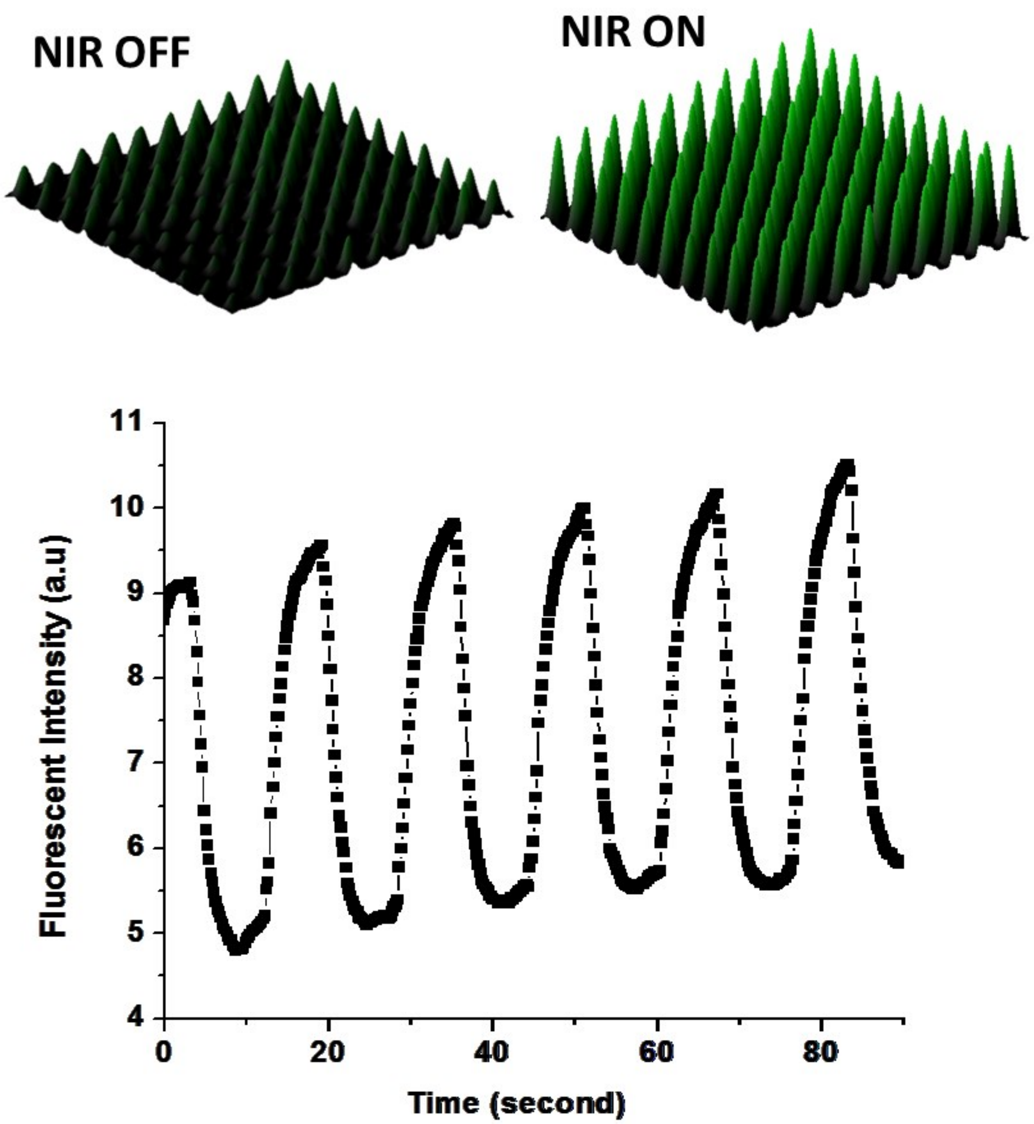
NIR OFF
NIR ON
Fluorescent Intensity (a.u)
Time (second)
11
10
9
8
7
6
5
4
0
20
40
60
80

Figure 11.

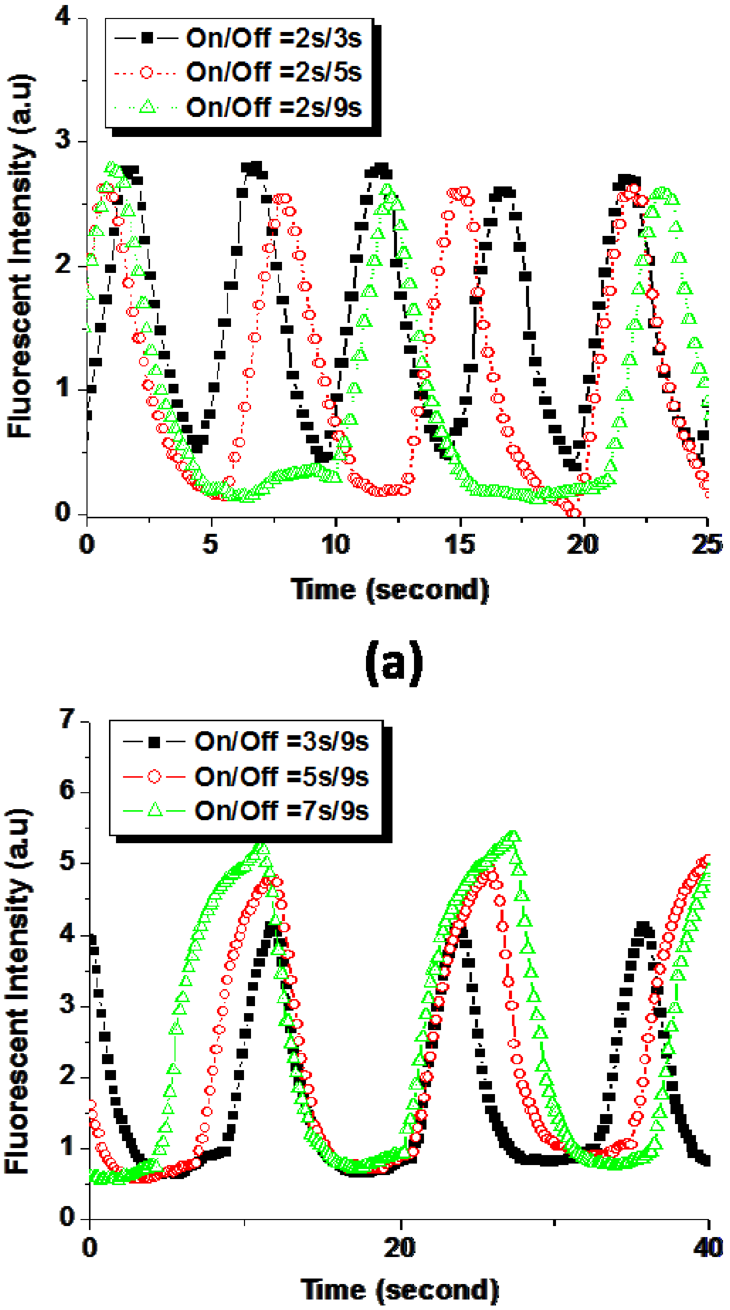

On/Off =2s/3s
On/Off =2s/5s
On/Off =2s/9s
Fluorescent Intensity (a.u)
0
1
2
3
4
0
5
10
15
20
25
Time (second)
(a)
On/Off =3s/9s
On/Off =5s/9s
On/Off =7s/9s
Fluorescent Intensity (a.u)
0
1
2
3
4
5
6
7
0
20
40
Time (second)

(b)

Table 1. Values of the model parameters used in the simulation

Water mass fraction	0.97
Water density [kg/m^3]	1000
Polymer density [kg/m^3]	1200
Water molecular weight [g/mol]	18
Water effective diffusivity in hydrogel [m^2/s]	1×10^{-9}
Elastic modulus of the relaxed hydrogel [kPa]	100
Elastic modulus of the unrelaxed hydrogel [kPa]	1000
Relaxation time of the hydrogel [s]	1000